# First studies of mesosphere and lower thermosphere dynamics using a multistatic specular meteor radar network over southern Patagonia

**J. Federico Conte[1], Jorge L. Chau[1], J. Miguel Urco[1], Ralph Latteck[1], Juha Vierinen[4], and Jacobo O. Salvador[2,3]**

[1]Leibniz Institute of Atmospheric Physics at the University of Rostock, Kühlungsborn, Germany
[2]Universidad Nacional de la Patagonia Austral, Ro Gallegos, Argentina
[3]CONICET, Argentina
[4]Arctic University of Norway, Tromsø, Norway

**Key Points:**

- First observations of MLT dynamics over the region of strongest stratospheric wave activity are analyzed.
- Estimates of mean horizontal winds and their gradients are possible, thanks to the multistatic configuration.
- Mean momentum fluxes are estimated with vertical velocity estimates free of horizontal divergence contamination.

Corresponding author: J. Federico Conte, `conte@iap-kborn.de`

## Abstract

This paper presents for the first time results on winds, tides, gradients of horizontal winds, and momentum fluxes at mesosphere and lower thermosphere (MLT) altitudes over southern Patagonia, one of the most dynamically active regions in the world. For this purpose, measurements provided by SIMONe Argentina are investigated. SIMONe Argentina is a novel multistatic specular meteor radar system that implements a SIMONe (Spread Spectrum Interferometric Multistatic meteor radar Observing Network) approach, and that has been operating since the end of September 2019. Average counts of more than 30000 meteor detections per day result in tidal estimates with statistical uncertainties of less than 1 m/s. Thanks to the multistatic configuration, horizontal and vertical gradients of the horizontal winds are obtained, as well as vertical winds free from horizontal divergence contamination. The daily averages of these preliminary results on the gradients are consistent with the expected MLT behavior during the summer and a strong southern hemisphere polar vortex. Mean momentum fluxes are estimated after removing the effects of mean winds using a four-hour, four-kilometer window in time and altitude, respectively. Reasonable statistical uncertainties of the momentum fluxes are obtained after applying a 28-day averaging. Therefore, the momentum flux estimates presented in this paper represent monthly mean values of waves with periods of four hours or less, vertical wavelengths shorter than four kilometers, and horizontal scales less than 400 km.


## 1 Introduction

The mesosphere and lower thermosphere (MLT) is the atmospheric region that couples the lower and upper parts of the terrestrial atmosphere. For this reason, knowledge of its dynamics is of great importance in order to understand the behavior of the atmosphere as a whole. The coupling is accomplished mainly via propagation of three dominant types of waves: planetary waves (PWs), tides and gravity waves (GWs). PWs are waves with scales of thousands of kilometers and periods of up to $\sim$ 30 days. They are mainly generated in the troposphere by land-sea discontinuities, or triggered in-situ by, e.g., baroclinic instabilities and filtered gravity waves (e.g., Rossby, 1939; McCormack et al., 2014; H.-L. Liu & Roble, 2002). Tides are also waves with horizontal scales of thousands of kilometers, but periods that are sub-harmonics of the solar and lunar days. Thermal tides are mainly a consequence of solar radiation absorption by water vapour in the troposphere and ozone in the stratosphere, while the lunar tide results from the gravitational pull of the Moon (e.g., Lindzen & Chapman, 1969; Forbes, 1984). GWs are small to medium scale waves with periods ranging from a few minutes to several hours. They can be triggered by a myriad of different sources, e.g., the orography, thunderstorms, shear instabilities, convection, etc. (e.g., Hines, 1988; Piani et al., 2000; Fritts & Alexander, 2003).

During the last decades, specular meteor radars (SMRs) have been extensively used to study winds and atmospheric waves in the MLT (e.g., Hocking, 2005; Clemesha et al., 2009; Hoffmann et al., 2010; A. Z. Liu et al., 2013; Laskar et al., 2016; Jia et al., 2018, and references therein). They have also been used to study GWs, which are known to play an important role in determining the wind and thermal structure of the MLT (e.g., Fritts, 1984). Particularly, some studies have focused on extracting information about GW-driven momentum fluxes from SMR measurements (e.g., Fritts et al., 2010; Placke et al., 2011a; Andrioli et al., 2015). However, understanding the results on momentum flux estimates based on SMR winds is not trivial, mainly because of the uncertainties associated with the estimation procedure (e.g., Fritts et al., 2012b). In fact, Vincent et al. (2010) showed that the accuracy in the momentum flux estimation is highly dependent on the number of meteor detections. Consequently, the usage of multistatic meteor radar systems represents one way to reduce the uncertainties of the momentum flux estimates (e.g., Spargo et al., 2019). Furthermore, by detecting more meteors and being able to observe them from different viewing points, multistatic SMR systems also allow for more reliable estimations of horizontal wind gradients.

The MLT over the southern part of Argentina and Chile is considered to be one of the most dynamically active regions in the globe. Satellite-based studies have revealed that GW-driven momentum fluxes increase considerably at both stratosphere and MLT altitudes over Patagonia (e.g., Trinh et al., 2018; Vadas et al., 2019a). Numerical model simulations have reported generation of secondary GWs with horizontal scales of up to 2000 km at mesospheric altitudes over the southern Andes (Vadas & Becker, 2019). Nevertheless, wave coupling processes in the MLT region over the Patagonian sector are still not well understood, partly because the installation of ground-based instruments has not been possible, either due to logistics challenges or instrument requirements. In this work, we present preliminary results of a multistatic SMR network that allows, for the first time, measurements of MLT dynamics in the Patagonian region. Besides the local support, our success has been possible thanks to a novel approach that we call SIMONe (Spread Spectrum Interferometric Multistatic meteor radar Observing Network) (Chau et al., 2019). SIMONe makes use of modern radar practices like spread-spectrum, MIMO (Multiple-Input, Multiple-Ouput), and compressed sensing applied to atmospheric radars (Vierinen et al., 2016; Urco et al., 2018, 2019). This allows for much easier installation, operation and expansion of the network than previous equivalent systems.

The paper is organized as follows. Section 2 introduces the SIMONe Argentina system. Section 3 provides a detailed description of the different analyses performed to the data. Then, we present and discuss the main results and findings in Section 4. Finally, in section 5 the concluding remarks are presented.

## 2 SIMONe Argentina

SIMONe Argentina is a state-of-the-art network of multistatic specular meteor radars that was installed in September of 2019 in the southern province of Santa Cruz, Argentina. It is comprised of one single transmitting site with five linearly polarized Yagi antennas in a pentagon configuration, and five receiving sites with one dual-polarization Yagi antenna each. The receivers are placed between 30 and 270 km of distance from the transmitting site, which is located at 49.6° S, 71.4° W (see Figure 1 for details on the geographical distribution of the sites). This type of network configuration is known as MISO (Multiple-Input, Single-Output), since only one antenna is used on reception (e.g., Chau et al., 2019).

SIMONe Argentina is the result of an effort led by the Leibniz Institute of Atmospheric Physics (Germany) in collaboration with the Universidad Nacional de la Patagonia Austral (Argentina), and the Artic University of Norway. A similar system has been installed in Peru (SIMONe Peru). SIMONe systems use coded spread spectrum on transmission (Vierinen et al., 2016). A phase coded signal based on pseudo-random sequences is generated and transmitted on each antenna independently. Transmission is done at a frequency of 32.55 MHz and with an average power of 400 W per antenna. All five transmitted codes are simultaneously decoded at each receiving site by means of compressed sensing (e.g., Urco et al., 2019). Hardware and software details of both systems, i.e., SIMONe Peru and SIMONe Argentina, can be found in Chau et al. (2020).

SIMONe Argentina started operations by the end of September 2019 and has been running since then with almost no interruptions. Figure 2 shows a summary of the detection statistics for the first seven months of operations. The upper panel indicates the normalized percentage of meteor counts for each individual link. The bottom panel is used to present the average daily total counts for each month. Problems with the local power supply at the transmitting site resulted in fewer meteor detections during April

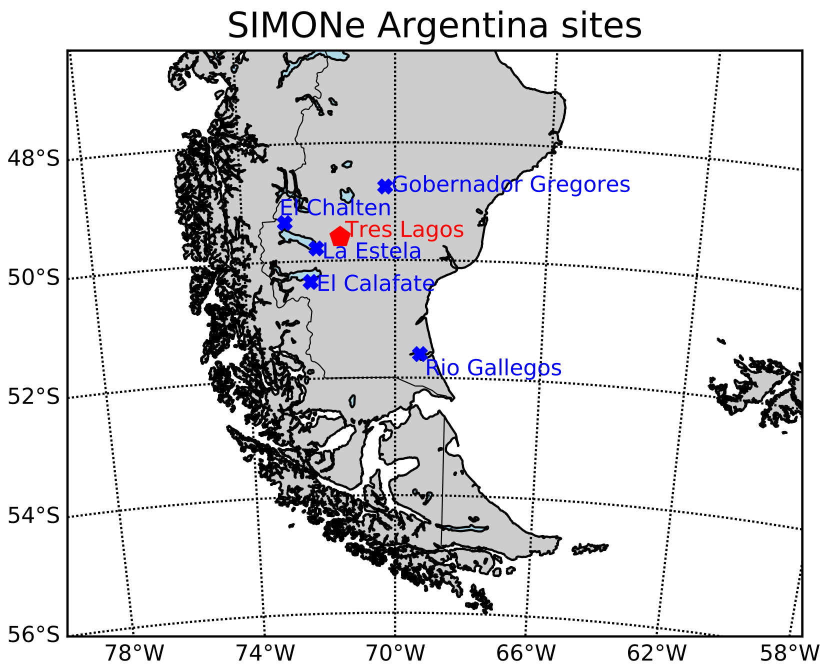


**Figure 1.** Map of SIMONe Argentina. The transmitter is indicated with the filled red pentagon, and the receivers are indicated with the blue crosses.

of 2020. Besides, the receiving site at Gobernador Gregores was out of operation during December of 2019 due to damage in the antenna cables. Nevertheless, for most of the time, the number of counts was much higher than in standard specular meteor radars. The links concentrating most of the meteor detections are Tres Lagos-El Calafate and Tres Lagos-La Estela. Starting in March 2020, the link Tres Lagos-Rio Gallegos exhibits a considerable increase in the counts, as a result of having rotated the transmitting antennas by 90 degrees. By month, January presents the largest counts, with an average of more than 50000 meteor detections per day.

## 3 Data analysis

Specular meteor radars (SMRs) are used to measure the Doppler shift of meteor trails due to their drifting with the mesospheric neutral winds (e.g., Jones et al., 1998). In order to extract the wind information from the measurements, one may implement an all-sky fit of the Doppler velocities measured during a certain period of time and within a given altitude interval (e.g., Hocking et al., 2001; Holdsworth et al., 2004). In other words, one must solve the following equation:

$$\mathbf{u} \cdot \mathbf{k} = 2\pi f + \zeta, \tag{1}$$

where $\mathbf{u} = (u, v, w)$ is the neutral wind vector, with $u$, $v$ and $w$ being its zonal (east-west), meridional (north-south) and vertical (up-down) components, respectively. $\mathbf{k} = (k_u, k_v, k_w)$ is the Bragg wave vector (scattered minus incident) in the meteor-centered east-north-up coordinate system (perpendicular to the meteor trail); $f$ is the Doppler shift; and $\zeta$ is the Doppler shift uncertainty. For this equation to be valid, one must make the assumption that the winds at each given height interval are uniform during the selected period of time (homogeneous method). The results using the homogeneous method have been obtained assuming $w = 0$.

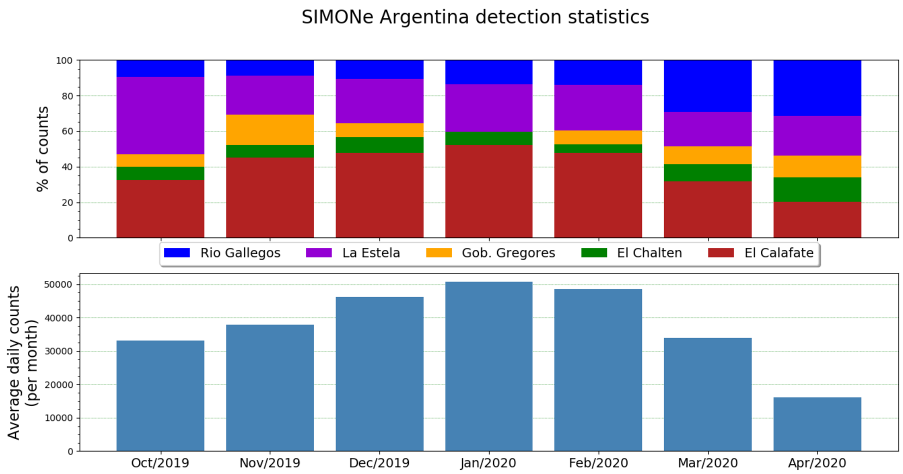


**Figure 2.** Upper panel: normalized percentage of meteor counts, color coded for each individual link. Bottom panel: monthly daily mean counts for all the links combined (see text for details).

Monostatic SMRs commonly allow for hourly horizontal wind estimations every 2-3 km in altitude (e.g., Jacobi et al., 1999; Hoffmann et al., 2010). The wind estimates are representative of mean values over an area of $\sim$ 200 km in radius. These horizontal winds can be further processed in order to obtain information about large scale waves such as planetary waves and tides (e.g., Murphy et al., 2006; Chau et al., 2015; Conte et al., 2018).

One of the advantages of using multistatic SMR networks is that the amount of meteor detections is significantly increased (e.g., Stober & Chau, 2015). During most of the time since it started operations, SIMONe Argentina has been capable of detecting more than 30000 meteors per day (see Figure 2). With such amounts of meteor detections, one can not only reliably estimate horizontal winds with higher time and vertical resolutions ($\sim$ 15 min and 1 km, respectively), but also investigate second order parameters such as the squares of the perturbation components of the radial velocities, i.e., the momentum flux components (e.g., Spargo et al., 2019). Another advantage multistatic SMR networks present is that they are capable of sampling the observed volume from different viewing angles. In this scenario, the increased number of meteor detections can be further exploited in order to estimate first-order derivatives of the horizontal winds, and in this way include in the estimation a mean vertical wind free of horizontal divergence contamination (e.g., Chau et al., 2017).

Below, we describe the main procedures used in this work, i.e., tidal estimation, wind estimation using a gradient method, and mean momentum flux estimation. For all three procedures, a first wind estimation is carried out in order to remove outliers. This means solving Equation 1 in bins of the same size as that used later on in each given procedure (e.g., 4 hour, 4 km in the gradient method); and then removing the radial velocities the values of which have a corresponding residual of more than 25 m/s. This first wind estimation is carried out only in those bins containing a minimum of 10 meteor detections.

### 3.1 Tidal estimation

Horizontal winds obtained from meteor radar measurements have been used for several decades to investigate tides and planetary waves in the MLT (e.g., Hocking & Thayaparan, 1997; Fritts et al., 2012a). Different mathematical techniques such as least squares or wavelet analysis can be applied to the wind data in order to extract the tidal information (e.g., Stening et al., 1997; Sandford et al., 2006; He et al., 2017). To avoid zero-padding or interpolating when encountering data gaps, a least squares approach was selected for this study.

After removing the outliers, Equation 1 was again fitted to the Doppler shift measurements. For this purpose, a weighted least squares (WLS) technique was implemented using bins of 1 hour and 2 km (in altitude), shifted by half an hour and 1 km, respectively. The inverse of the squared Doppler shift uncertainties ($\zeta$ in Eq. 1) were used as weights. The WLS was carried out only in those bins containing a minimum of 10 meteor detections. Then, under the assumption that the obtained hourly horizontal winds are the result of the superposition of a mean wind and different period oscillations, the following equation was fitted to the zonal ($u$) and meridional ($v$) wind components

$$[u + \psi_u, v + \psi_v] = [U_0, V_0] + \sum_{i=1}^{4} [A_u, A_v]_i \cos\Big(2\pi \frac{(t - [\phi_u, \phi_v]_i)}{T_i}\Big). \tag{2}$$

Here, $\psi_u$ and $\psi_v$ are the Doppler shift uncertainties (error) propagated into the estimated winds; $U_0$ and $V_0$ are the mean zonal and meridional winds; $\mathrm{A}_{u_i}$ ($\mathrm{A}_{v_i}$) and $\phi_{u_i}$ ($\phi_{v_i}$) are the amplitude and phase, respectively, of the zonal (meridional) component of each considered wave; $T_1 = 2$ day; $T_i$ for $i > 1$ is the period of each considered tide ($T_2 = 24$ h, $T_3 = 12$ h and $T_4 = 8$ h, for the diurnal, semidiurnal and terdiurnal solar tides, respectively); and $t$ is the Universal Time (UT) in hours. The cosine of a sum was used to linearize Equation 2, which then was solved by applying the WLS method using a running window of 4 days shifted by 1 day.

### 3.2 Wind field gradient method

If one relaxes the assumption of homogeneity, the wind field inside the observed area may be estimated using the gradient method. This method consists in approximating the horizontal winds with their first-order Taylor expansion terms (e.g., Burnside et al., 1981; Browning & Wexler, 1968; Chau et al., 2017). This means introducing the following expression into Equation 1

$$\mathbf{u} = \mathbf{u}_0 + \mathbf{u}_x(x - x_0) + \mathbf{u}_y(y - y_0) + \mathbf{u}_z(z - z_0), \tag{3}$$

where $\mathbf{u}_0 = (u_0, v_0, w_0)$ represents the mean wind; $\mathbf{x}_0 = (x_0, y_0, z_0)$ is a reference point; and

$$\begin{aligned} \mathbf{u}_x &= \Big(\frac{du}{dx}, \frac{dv}{dx}, \frac{dw}{dx}\Big) \\ \mathbf{u}_y &= \Big(\frac{du}{dy}, \frac{dv}{dy}, \frac{dw}{dy}\Big) \\ \mathbf{u}_z &= \Big(\frac{du}{dz}, \frac{dv}{dz}, \frac{dw}{dz}\Big). \end{aligned}$$

The coordinates $(x, y, z)$ are in km, and calculated taking into consideration the latitude, longitude and altitude of each meteor detection and the radius of the Earth at the reference point. $\mathbf{x}_0$ is determined using the latitude and longitude of the transmitting site, and the altitude of each height level considered in the WLS fit. The latter was implemented using bins of 4 hour and 4 km (in altitude), shifted by half an hour and 1 km, respectively. For this study, we have assumed that $(dw/dx,\, dw/dy,\, dw/dz) = \mathbf{0}$, which means solving for nine unknowns. In this method, a conservative condition of having a minimum of eighty one meteor detections per bin was selected.

### 3.3 Momentum flux estimates

The procedure followed in this study to estimate the GW momentum flux is based on the works by Thorsen et al. (1997) and Hocking (2005). It consists in applying a least square method to solve the following equation

$$(\mathbf{u}' \cdot \mathbf{k})^2 = (2\pi(f - \hat{f}))^2. \tag{4}$$

In this expression, $\mathbf{k}$ and $f$ are, respectively, the same Bragg wave vector and same Doppler shift as in Equation 1, but $\mathbf{u}'$ represents the perturbed wind vector instead. $\hat{f}$ is a so-called mean Doppler shift,

$$\hat{f} = \mathbf{u} \cdot \mathbf{k}/2\pi, \tag{5}$$

where $\mathbf{u}$ is the mean wind that results from solving Equation 1 or 3. To guarantee more reliable values of the six unknowns (<u'u'>, <v'v'>, <u'w'>, <v'w'>, <u'v'> and <w'w'>), the fit was performed only in those bins containing forty meteor detections or more.

From Equation 5, it follows that different momentum flux estimates may be obtained depending on the mean wind that is used to determine $\hat{f}$. In this study, the wind estimates that result from the gradient method were used to calculate $\hat{f}$ (see previous section). That is, Equation 3 (with $dw/dx = dw/dy = dw/dz = 0$) was introduced into Equation 1, and the latter then solved using bins of 4 hour and 4 km, shifted by 30 min in time and 1 km in altitude. Finally, Equation 4 was solved in bins of 1 hour and 2 km (in altitude), shifted by 30 min and 1 km, respectively.

## 4 Results and discussion

One of the main goals of this work is to provide, for the first time, information on the MLT dynamics over southern Patagonia obtained using SIMONe Argentina. For this reason, our results are discussed as they are presented.

### 4.1 Mean winds and tides

In Figure 3, we present the mean zonal ($U_0$) and meridional ($V_0$) winds, and the total amplitudes of the quasi two-day planetary wave (Q2DW) and the diurnal (D1), semidiurnal (S2) and terdiurnal (T3) solar tides. The vertical black dashed line indicates January 1st 2020. The term *total amplitude* refers to the magnitude of the vector sum of the corresponding zonal and meridional components of each fitted wave. The statistical uncertainties of the estimated parameters are shown in the right column panels. All quantities were obtained after applying the procedure detailed in Section 3.1. Data gaps are shown in white.

From inspection of Figure 3, two features stand out: the S2 tide is the dominant wave, with amplitudes in the order of 40-65 m/s, and the Q2DW exhibits strong enhancements after 4 January 2020. It is well known that the semidiurnal solar tide at middle latitudes dominates over all other tidal components (e.g., Andrews et al., 1987; Pancheva & Mukhtarov, 2011). Furthermore, many studies of tides in the northern hemisphere (NH) have reported that S2 decreases significantly around the onset of a sudden stratospheric warming (SSW) event, to later on recover and reach even larger amplitudes than those exhibited prior to the SSW (e.g., Chau et al., 2015; Siddiqui et al., 2018; Conte et al., 2019). In September of 2019, approximately 12 days before the 27th (first day of available data from SIMONe Argentina), a SSW event was registered in the southern hemisphere (e.g., Yamazaki et al., 2020). Interestingly enough, the largest amplitudes of S2 are seen between 27 September and 12 October, which might be an indicative of the recovery phase of S2 after the weakening associated with a SSW event. For the entire dataset analyzed in this study, S2 exhibits significant intraseasonal variability, which becomes evident in the many, although weaker, enhancements observed after $\sim$ 31 October.

The Q2DW at middle latitudes has been reported to reach maximum amplitudes during the summer (e.g., Kumar et al., 2018). In our results, the Q2DW is active mostly in summer, in agreement with previous studies. Even more, it becomes the dominant wave by the end of January 2020, with amplitudes larger than those corresponding to S2. Offermann et al. (2011) showed that the Q2DW exhibits a triple peak structure in the NH during summer. Although it may not be obvious at first, after a more through inspection of Figure 3, it can be noticed that the largest amplitudes of the Q2DW are distributed in three subsequent enhancements, around 7, 13 and 19 January. A fourth enhancement can be seen around 9 February, but the latter is significantly weaker than the previous three.

Both the diurnal and terdiurnal solar tides exhibit considerable intraseasonal variability. In the case of D1, its activity becomes more evident mostly below $\sim$ 90 km and during summer. Above $\sim$ 92 km, and mainly during equinox times, T3 becomes more noticeable, with amplitudes similar to those corresponding to D1.

Compared to five-year average values at 54° S presented by Conte et al. (2017), the summer reversal of the mean zonal wind shown in Figure 3 is observed at altitudes approximately two km lower. This is consistent with previous studies reporting a decrease with latitude of the height of the zonal wind summer reversal (e.g., Hoffmann et al., 2010; Wilhelm et al., 2019). Besides, it might seem that $U_0$ starts the transition into summer conditions relatively early, around 3 October. However, above $\sim$ 92 km, $U_0$ experiences a late reversal to westward conditions around 24 October, to finally go into summer conditions (i.e., eastward above the mesopause) about five days later. $V_0$ blows mainly towards the equator, and only after 10 March poleward values start to dominate.

The statistical uncertainties of all the fitted parameters presented in Figure 3 are very small. Only above 103 km and below 77 km, values of $\sim$ 2-3 m/s are obtained (not shown). The low statistical uncertainties are a consequence of the large amount of meteor detections provided by SIMONe Argentina. By solving Equation 1 in bins of one hour and two km, one guarantees wind estimates with very low uncertainties. The latter, combined with the fact the WLS method used to solve Equation 2 is applied to a very well conditioned matrix, results in small statistical uncertainties.

### 4.2 Gradients and vertical wind

In Figure 4, we present the winds and gradients obtained after applying the procedure described in Section 3.2. Given that we want to minimize the effects that tides may have on the gradients, only daily averages are presented. The first four panels on the left show the mean zonal wind and the mean zonal eastward, northward and upward derivatives, i.e., $u_0$, $u_x$, $u_y$ and $u_z$, respectively. The corresponding four panels on the right show the mean meridional wind and mean meridional first-order derivatives, i.e., $v_0$, $v_x$, $v_y$ and $v_z$, respectively. The fifth panel is reserved to show the mean vertical wind ($w_0$) on the left, and its statistical uncertainty ($\sigma(w_0)$) on the right. The gradients are in m/s/km, while the remaining parameters are in m/s. Data gaps are shown in white.

Before starting the description of the main features observed in Figure 4, it is important to stress here that the variability seen in the mean winds is representative of large scale structures, with periods greater than four hours and vertical wavelengths larger than four km. $u_0$ and $v_0$ do not differ much from the mean winds shown in Figure 3. They do show more variability, although this is expected since $u_0$ and $v_0$ are daily averages of 4-hour winds, while the $u$ and $v$ presented in the previous section are 4-day mean winds. Part of this variability may be attributed to the Q2DW, which becomes noticeable around 5 January in $u_0$, and around 25 January in the case of $v_0$.

Some previous observational studies have investigated the horizontal gradients in the zonal and meridional winds (e.g., Conde & Smith, 1998; Meriwether et al., 2008; Chau et al., 2017). However, the present study is the first one to show results on both the hor-

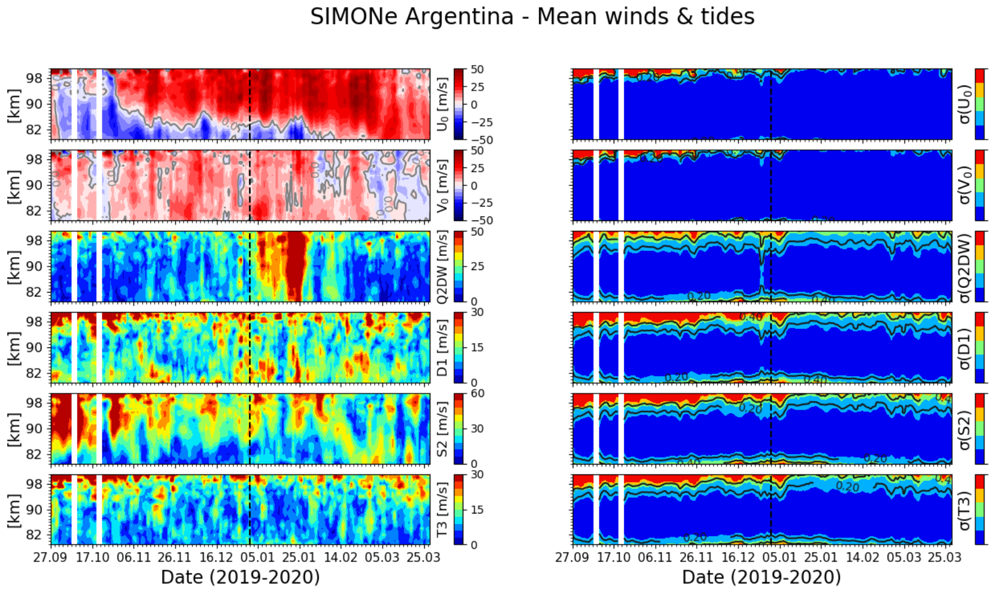


**Figure 3.** Mean zonal ($U_0$) and meridional ($V_0$) winds, the quasi two-day planetary wave (Q2DW), and the diurnal (D1), semidiurnal (S2) and terdiurnal (T3) solar tides during September 2019 - April 2020 over SIMONe Argentina. The corresponding statistical uncertainties (in m/s) are shown in the right column. All parameters were estimated using a four-day running window shifted by one day. The vertical black dashed line indicates January 1st 2020.

izontal and vertical gradients of MLT horizontal winds over southern Patagonia. From Figure 4, it can be seen that $u_x$ and $v_y$ have amplitudes that, when added together, may result in values of $u_x+v_y$ in the order of $\sim$ 0.4 m/s/km. Chau et al. (2017) showed that horizontal divergence values of $\sim$ 0.1 m/s/km are large enough to introduce an apparent vertical wind of 1-2 m/s. Consequently, one can now understand the importance of estimating the vertical wind together with the gradients. By doing the latter, one reduces significantly the effects of biases introduced in $w_0$ by horizontal variability of $u$ and $v$. On the other hand, $u_x$ is expected to be zero (on average) during the summer. After computing the mean over longer intervals of time (e.g., 10 days) and hence averaging out long period waves typical of summer, such as the Q2DW, $u_x$ becomes indeed very small, with values of $\sim$ 0.01-0.03 m/s/km and mainly negative above $\sim$ 82 km, and positive below (not shown here).

In the case of $u_y$ and $v_x$, daily amplitude values are in the order of 0.3 m/s/km. The larger amplitudes of $u_y$ (compared to $u_x$) may be an indicative of zonal wind latitudinal changes related to the SH polar vortex, part of which usually locates below the region seen by SIMONe Argentina (e.g., Figure 8 in Orte et al. (2019)). For altitudes lower than $\sim$ 84 km, $u_y$ ($v_x$) is mainly negative (positive). The upward component of the relative vorticity can be coarsely approximated by $v_x-u_y$ (for a precise calculation, one needs to include the latitude information; see Equation A16 in Chau et al. (2017)). Notice that below $\sim$ 84 km, $v_x-u_y$ is mainly positive, which suggests an upward movement due to vortical effects. Besides, differences between the amplitudes of $u_y$, $v_x$ and $u_x$, $v_y$, suggest that changes in the horizontal gradients due to GWs depend on the propagation direction of the these waves.

The vertical gradients of both the zonal and the meridional wind components, i.e., $u_z$ and $v_z$, show the largest amplitudes of all the first-order derivatives analyzed in this work. Between 81 and 90 km of altitude, and during approximately the same period of time the zonal wind summer reversal is observed, $u_z$ shows strong positive amplitudes ($\sim$ 15 m/s/km or more). During the summer, the zonal wind decreases with the altitude. This negative vertical gradient of the zonal wind allows eastward propagating GWs to easily reach mesospheric altitudes, where they break and deposit momentum and energy. This deposition of momentum creates an eastward drag that decelerates the zonal (westward) wind. Due to the Coriolis effect, the deceleration of the zonal wind introduces an equatorward meridional wind component, which in turn leads to an upward motion and a subsequent (adiabatic) cooling of the mesopause region (e.g., Smith, 2012). Finally, due to the thermal wind equation, $u_z \approx -\partial T/\partial y$ (where $y$ is the latitude, and $T$ is the temperature), the adiabatic cooling results in the positive values of $u_z$ seen in Figure 4. In the case of $v_z$, the amplitudes are in the order of $\sim$ 10 m/s/km. Besides, there is considerable day-to-day variability, although no clear pattern or structure in time can be noticed.

The mean vertical wind ($w_0$) exhibits large amplitudes, with values in the order of $\sim$ 6-11 m/s. This study is not the first one to report large amplitudes in the mean vertical winds estimated using SMRs. For example, Babu et al. (2012) and Egito et al. (2016) reported that the vertical winds at low latitudes may reach magnitudes of 6-10 m/s. In our study, the maximum amplitudes are observed mostly above 90 km of altitude. Notice that below 90 km, $w_0$ is predominantly positive during the summer, and only becomes predominantly negative after 25 January, when eastward values of $u_0$ start to dominate at all height levels above 81 km. It is important to stress again that, by estimating $w_0$ together with the first-order derivatives, possible contamination by the horizontal gradients is removed. In Figure 4, we only present the statistical uncertainties of $w_0$, because they happen to be the largest ones (for the other estimates, the largest values of the *relative* $\sigma$ are in the order of 5-7 %). Note that only for altitudes above 96 km and below 79 km, where the number of meteor detections is lower, $\sigma(w_0)$ exceeds values of 1 m/s.

It is of interest mentioning that mostly above 90 km of altitude, and during certain days of the summer, the 4-hour $w_0$ estimates (without computing the daily mean) exhibit a clear diurnal pattern (not shown here). Similar diurnal oscillations in $w_0$, and also in the horizontal gradients are reported in Chau et al. (2020). Exploring diurnal and other period oscillations that may be present in the vertical winds will be the focus of a future study.

### 4.3 Gravity-wave-driven momentum flux

We now present and discuss the momentum flux estimates obtained after subtracting the mean winds calculated following the gradient method, i.e., the $u_0$, $v_0$ and $w_0$ that were estimated together with the gradients. In Figure 4, it can be seen that the horizontal wind gradients and the vertical mean wind exhibit considerable variability, both in time and altitude. Part of this variability is leaked into the mean horizontal winds when one solves Equation 1 without including the gradients and $w_0$ in the wind vector $\mathbf{u}$. This implies that the $u_0$, $v_0$, $w_0$ obtained using the gradient method constitute a better representation of the real mean wind, provided that enough meteors are detected in order to accomplish a robust wind estimation. Besides, it is important to have in mind that the subtracted winds were estimated in bins of 4 hour and 4 km (in altitude). This means that the corresponding momentum flux estimates are representative mostly of waves with temporal and vertical scales of less than 4 hour and 4 km, respectively.

In Figure 5, we present 28-day averages of the momentum flux estimates that result from subtracting the $\hat{f}$ that was calculated using the $u_0$, $v_0$, $w_0$ discussed in the previous paragraph (see Equation 4). The averages were calculated over 28 days in order to obtain estimates that are statistically more significant. The upper panels present $U$

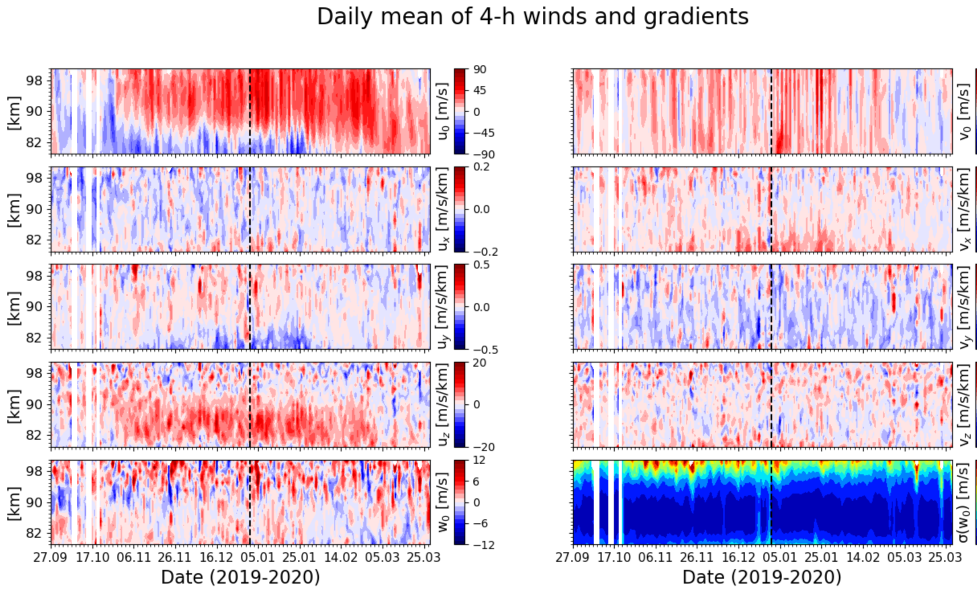


**Figure 4.** Daily averages of: (first panel) mean zonal ($u_0$) and meridional ($v_0$) winds, (second panel) eastward zonal ($u_x$) and meridional ($v_x$) derivatives, (third panel) northward zonal ($u_y$) and meridional ($v_y$) derivatives, and (fourth panel) upward zonal ($u_z$) and meridional ($v_z$) derivatives. The mean vertical wind ($w_0$) and its statistical uncertainty ($\sigma(w_0)$) are also included (bottom panel). All parameters were estimated using a 4 hour, 4 km (in vertical) bin, shifted by 30 min and 1 km, respectively. The vertical black dashed line indicates 1 January 2020.

and $V$, which correspond to the 28-day averages of the mean zonal and meridional winds, respectively. The middle panels are used to show the 28-day mean horizontal momentum vertical fluxes, <u'w'>, <v'w'>. The statistical uncertainties of <u'w'> and <v'w'>, i.e., $\sigma$(u'w') and $\sigma$(v'w'), respectively, are shown in the bottom panels.

Momentum flux estimations based on SMR observations were first presented by Hocking (2005). Since then, several studies have investigated momentum fluxes using meteor radar winds (e.g., Fritts et al., 2010; Placke et al., 2011b; Fritts et al., 2012b; Andrioli et al., 2013; Placke et al., 2015, and references therein). More recently, de Wit et al. (2016) observed a modulation by the quasi-biennial oscillation (QBO) of the momentum fluxes over Tierra del Fuego, an island south of Santa Cruz province. Typical amplitudes of <u'w'> and <v'w'> reported in these previous studies rarely reach values larger than 60-70 $m^2/s^2$. Using a multistatic meteor radar network over southern Australia, Spargo et al. (2019) observed values for <u'w'> and <v'w'> in the order of 40-50 $m^2/s^2$, which are larger than momentum flux absolute values obtained from satellite measurements (e.g., Ern et al., 2011; Trinh et al., 2018). The latter is most likely due to observational features inherent to satellites.

From Figure 5, it can be seen that our momentum flux estimates have amplitudes in the order of 40-60 $m^2/s^2$. Some large amplitudes of more than 100 $m^2/s^2$ can be observed above 97 km of altitude, where the corresponding statistical uncertainties are in the order of 50 $m^2/s^2$ (see bottom panels). Both momentum flux estimates exhibit variability in time and height, although it is more evident in the case of <u'w'>. Notice that despite the 28-day averaging, the magnitudes of <u'w'> and <v'w'> are considerable throughout the entire period of time analyzed in this study. Momentum flux estimates averaged over 20 days presented by Placke et al. (2015) exhibit maximum amplitudes of 6-8 $m^2/s^2$ during the summer of the northern hemisphere. The largest amplitudes of ten-day momentum flux estimates shown by Spargo et al. (2019) reach values of 30-40 $m^2/s^2$ in the beginning of the spring of the southern hemisphere. Compared to these studies, it is clear that the wave activity in the MLT region over the Patagonian sector is very strong. The latter is consistent with previous studies based on satellite measurements (e.g., Ern et al., 2011), and numerical simulations (e.g., Lund et al., 2020).

As GWs propagate upwards, they transfer momentum and energy into the mean flow. Consequently, a decrease in the vertical flux of zonal momentum should correspond with an increase in the zonal wind speed (e.g., Fan et al., 1991). In other words, the mean zonal wind and <u’w’> should have opposite signs, i.e., <u’w’> positive in summer and negative during the winter. Our results are consistent with this reasoning, since for altitudes below 90-92 km, <u’w’> is mainly positive until $\sim$ 24 February. Furthermore, these positive <u’w’> amplitudes exhibit a vertical gradient: as the altitude increases, they progressively decrease from values of around 90 $m^2/s^2$ below 82 km, to values of $\sim$ 10 $m^2/s^2$ above 90 km. The latter is also consistent with the results on $u_z$ presented in the previous section. Besides, note that after 22 February, negative values of <u’w’> start to develop below 90-91 km. At that time of the year, $U$ has become eastward at all altitudes observed by SIMONe, a condition that allows westward propagating GWs to reach higher altitudes and, most likely, induce the aforementioned <u’w’> negative values.

In the case of <v’w’>, an upward movement of southward momentum dominates mostly below $\sim$ 91 km, from the beginning of October until the end of March. During the last week of December 2019, positive values of <v’w’> start to dominate above 92-94 km, an altitude range that had been dominated by negative values of <v’w’> since the beginning of November 2019. During the latter, and approximately above 96 km of altitude, an upward movement of eastward momentum can be noticed again. These positive values of <u’w’> develop very abruptly around 26 November, and remain dominant above 95 km for more than 25 days. We wonder if this might be an indicative of eastward momentum deposition by GWs that were in-situ generated at altitudes above 90 km.

To finalize, we discuss the procedure followed to estimate $\sigma$(u’w’) and $\sigma$(v’w’), and the reason for calculating 28-day averages. Unless one knows with some degree of certainty that a given wave event has occurred, the effects of GWs should be treated as stochastic processes. In other words, the mean momentum flux estimates are highly dependent on the effects of the geophysical variability. Kudeki and Franke (1998) showed that in order to obtain statistically significant momentum flux estimates at mesospheric heights, one must consider averaging intervals of more than 25 days. Specifically, they found that the statistical uncertainty of <u’w’> can be approximated with:

$$\sigma(u'w') = \sqrt{\frac{(< u'u' >)(< w'w' >)}{T/\tau}}, \tag{6}$$

where, <u’u’> and <w’w’> are averaged over the interval of time $T$; and $\tau$ is equal to half of the mesosphere Brunt-V$\ddot{a}$is$\ddot{a}$l$\ddot{a}$ period ($\sim$ 7 min). $\sigma$(v’w’) is obtained using same Equation 6, but replacing <u’u’> by <v’v’>. Selection of an averaging window $T$ = 28 days resulted in the values presented in Figure 5. In this way, the <u’w’> and <v’w’> obtained from our study must be understood as representatives of a monthly mean momentum flux due to waves with periods of 4 h or less, and horizontal scales less than 400 km. Besides, for those estimates corresponding to altitudes lower than $\sim$ 98 km, statistical uncertainties between 2-3 and 35 $m^2/s^2$ should be taken into consideration.

The momentum flux estimates are also affected by the correlated Doppler shift errors. In other words, because the Doppler shift uncertainties are squared when introduced into Equation 4, the resulting momentum flux estimates are in fact an overestimation

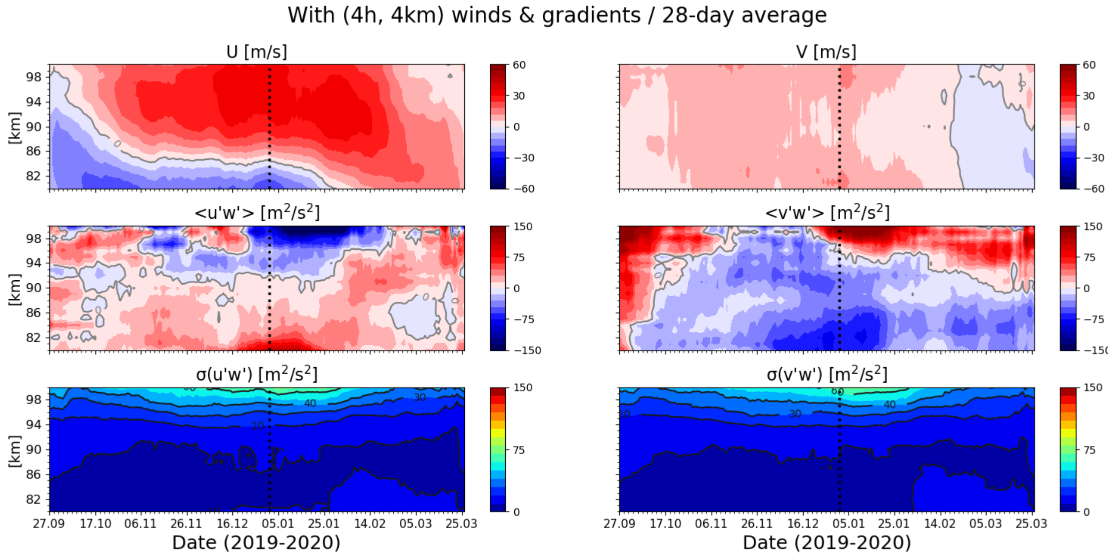


**Figure 5.** 28-day averages of 4-h, 4-km mean zonal and meridional winds (U and V, respectively), horizontal momentum vertical fluxes (<u'w'>, <v'w'>) and their corresponding statistical uncertainties ($\sigma$(u'w'), $\sigma$(v'w')). 4 hour, 4 km (in altitude) mean horizontal and vertical winds estimated in combination with the gradients (i.e., the $u_0$, $v_0$, $w_0$ described in Section 3.2) were subtracted before estimating the momentum flux. The vertical black dashed line indicates 1 January 2020.

of the real <u'w'> and <v'w'> (Vierinen et al., 2019). However, given that the Doppler shift uncertainties we obtained are small and that the amplitudes of <u'w'> and <v'w'> are large, the effects of the correlated errors were neglected in this study. We plan to further investigate this issue by extending our analysis to include non-zero lag second-order statistics of the wind velocities.

## 5 Concluding remarks

The first multistatic meteor radar based studies of mean winds, tides, gradients and momentum flux over the southern part of Patagonia have been presented in this paper. By doing this, we have demonstrated the ability of SIMONe Argentina to obtain not only information on typical MLT parameters such as mean winds and tides, but also to successfully estimate previously little investigated parameters, such as horizontal and vertical gradients of the horizontal winds. Using the latter, one can estimate, e.g., the horizontal divergence and the relative vorticity, parameters from which global circulation models can benefit and in this way help to further the understanding of MLT dynamics.

Our results show a strong positive vertical gradient in the zonal wind during the summer, in agreement with the residual mean meridional circulation. Besides, the horizontal gradients of the zonal and meridional winds seem to indicate possible effects of the southern hemisphere polar vortex. The mean vertical wind ($w_0$) has also been estimated, but only when the horizontal and vertical gradients were taken into account. The amplitudes obtained for $w_0$ are larger than expected ($\sim$ 10-15 m/s).

Momentum fluxes, <u'w'> and <v'w'>, have been estimated after removal of horizontal and vertical mean winds that were fitted together with the wind gradients. Compared to some previous studies, our momentum flux estimates exhibit larger amplitudes, which indicates that the GW activity in the MLT over southern Patagonia is very strong. The statistical uncertainties of <u'w'> and <v'w'> were also included in the analysis. The latter reveal that in order to have statistically significant momentum flux estimates, one should consider averages of at least 28 days. In this way, our results must be considered as representative of monthly mean momentum fluxes, driven by waves with periods shorter than 4 hours, vertical wavelengths shorter than 4 km, and horizontal scales less than 400 km.

We are confident that SIMONe Argentina has also the potential to investigate non-zero lag second-order statistics of MLT wind velocities, e.g., by using correlation function techniques such as those presented in Vierinen et al. (2019). This will be explored in future studies. Besides, we also plan to investigate momentum flux estimates without averaging over long periods of time, provided there is evidence of specific (deterministic) wave events occurring in the troposphere/stratosphere.

## Acknowledgments

The authors deeply thank Nico Pfeffer, Matthias Clahsen, Jens Wedrich and Thomas Barth (at IAP) for their invaluable help and expertise during the installation of SIMONe Argentina; and Jonathan Quiroga and Nahuel Daz (CONICET) for helping with the logistics prior to the installation. The authors would also like to thank Daro Godoy and Facundo Olivares (at Tres Lagos); Pablo Quiroz (at La Estela); Martn el griego Palopoli and National Parks staff (at El Chaltn); the Consejo Agrario de la Provincia de Santa Cruz (at Gob. Gregores and El Calafate); and the BAM-GAL (Argentina Air Force) for their support and help in maintaining the sites.

This work was partially supported by the Deutsche Forschungsgemeinschaft (DFG, German Research Foundation) under SPP 1788 (DynamicEarth) CH 1482/2, and by the Bundeministerium für Bildung und Forschung via project WASCLIM-IAP part of the ROMIC-II program.

The data used to produce the figures can be obtained in HDF5 format from ftp://ftp.iap-kborn.de/data-in-publications/ConteESS2020.

## References

Andrews, D. G., Holton, J. R., & Leovy, C. B. (1987). Middle atmosphere dynamics. *Academic Press, San Diego, California*. doi: 10.1002/qj.49711548612

Andrioli, V. F., Batista, P. P., Clemesha, B. R., Schuch, N. J., & Buriti, R. A. (2015). Multi-year observations of gravity wave momentum fluxes at low and middle latitudes inferred by all-sky meteor radar. *Ann. Geophys.*, *33*, 1183–1193. doi: 10.5194/angeo-33-1183-2015

Andrioli, V. F., Fritts, D. C., Batista, P. P., & Clemesha, B. R. (2013). Improved analysis of all-sky meteor radar measurements of gravity wave variances and momentum fluxes. *Ann. Geophys.*, *31*, 889–908. doi: 10.5194/angeo-31-889-2013

Babu, V. S., Ramkumar, G., & John, S. R. (2012). Seasonal variation of planetary wave momentum flux and the forcing towards mean flow acceleration in the MLT region. *J. Atmos. Sol. Terr. Phys.*, *78-79*, 53–61. doi: 10.1016/j.jastp.2011.05.010

Browning, K. A., & Wexler, R. (1968). The determination of kinematic properties of a wind field using Doppler radar. *J. Appl. Meteorol.*, *7*(1), 105–113.

Burnside, R. G., Herrero, F. A., Meriwether, J. W., & Walker, J. C. G. (1981). Optical observations of thermospheric dynamics at Arecibo. *J. Geophys. Res.*, *86*, 5532–5540.

Chau, J. L., Hoffmann, P., Pedatella, N. M., Matthias, V., & Stober, G. (2015). Upper mesospheric lunar tides over middle and high latitudes during sudden stratospheric warming events. *J. Geophys. Res.: Space Phys.*, *120*(4), 3084–3096. doi: 10.1002/2015JA020998

Chau, J. L., Stober, G., Hall, C. M., Tsutsumi, M., Laskar, F. I., & Hoffmann, P. (2017). Polar mesospheric horizontal divergence and relative vorticity measurements using multiple specular meteor radars. *Radio Sci.*, *52*, 811–828. doi: 10.1002/2016RS006225

Chau, J. L., Urco, J. M., Vierinen, J., Harding, B. J., Clahsen, M., Pfeffer, N., ... Erickson, P. J. (2020). Multistatic specular meteor radar network in Peru: System description and initial results. *Earth and Space Science*.

Chau, J. L., Urco, J. M., Vierinen, J. P., Volz, R. A., Clahsen, M., Pfeffer, N., & Trautner, J. (2019). Novel specular meteor radar systems using coherent MIMO techniques to study the mesosphere and lower thermosphere. *Atmospheric Measurement Techniques*, *12*(4), 2113–2127. doi: 10.5194/amt-12-2113-2019

Clemesha, B. R., Batista, P. P., Buriti da Costa, R. A., & Schuch, N. (2009). Seasonal variations in gravity wave activity at three locations in Brazil. *Ann. Geophys.*, *27*, 1059–1065. doi: 10.5194/angeo-27-1059-2009

Conde, M., & Smith, R. W. (1998). Spatial structure in the thermospheric horizontal wind above Poker Flat, Alaska, during solar minimum. *J. Geophys. Res.*, *103*, 9449–9472. doi: 10.1029/97JA03331

Conte, J. F., Chau, J. L., Laskar, F. I., Stober, G., Schmidt, H., & Brown, P. (2018). Semidiurnal solar tide differences between fall and spring transition times in the Northern Hemisphere. *Ann. Geophys.*, *36*, 999–1008. doi: 10.5194/angeo-36-999-2018

Conte, J. F., Chau, J. L., & Peters, D. H. W. (2019). Middle- and high-latitude mesosphere and lower thermosphere mean winds and tides in response to strong polar-night jet oscillations. *J. Geophys. Res.*, *124*, 9262–9276. doi: 10.1029/2019JD030828

Conte, J. F., Chau, J. L., Stober, G., Pedatella, N., Maute, A., Hoffmann, P., ... Murphy, D. J. (2017). Climatology of semidiurnal lunar and solar tides at middle and high latitudes: Interhemispheric comparison. *J. Geophys. Res.*, *122*. doi: 10.1002/2017JA024396

de Wit, R. J., Janches, D., Fritts, D. C., & Hibbins, R. E. (2016). QBO modulation of the mesopause gravity wave momentum flux over Tierra del Fuego. *Geophys. Res. Lett.*, *43*, 4049–4055. doi: 10.1002/2016GL068599

Egito, F., Andrioli, V. F., & Batista, P. P. (2016). Vertical winds and momentum fluxes due to equatorial planetary scale waves using all-sky meteor radar over Brazilian region. *J. Atmos. Sol. Terr. Phys.*, *149*, 108–119. doi: 10.1016/j.jastp.2016.10.005

Ern, M., Preusse, P., Gille, J. C., Hepplewhite, C. L., Mlynczak, M. G., Russell III, J. M., & Riese, M. (2011). Implications for atmospheric dynamics derived from global observations of gravity wave momentum flux in stratosphere and mesosphere. *J. Geophys. Res.*, *116*. doi: 10.1029/2011JD015821

Fan, Y., Klostermeyer, J., & Rüster, R. (1991). VHF radar observation of gravity wave critical levels in the mid-latitude summer mesopause region. *Geophys. Res. Lett.*, *18*, 697–700.

Forbes, J. M. (1984). Middle atmosphere tides. *J. Atmos. Terr. Phys.*(46), 1049–1067.

Fritts, D. C. (1984). Gravity wave saturation in the middle atmosphere: A review of theory and observations. *Rev. Geophys.*, *22*, 275–308.

Fritts, D. C., & Alexander, M. J. (2003). Gravity wave dynamics and effects in the middle atmosphere. *Reviews of Geophysics*, *41*(1). doi: 10.1029/2001RG000106

Fritts, D. C., Iimura, H., Lieberman, R., Janches, D., & Singer, W. (2012a). A conjugate study of mean winds and planetary waves employing enhanced meteor radars at Rio Grande, Argentina (53.8°S) and Juliusruh, Germany (54.6°N). *J. Geophys. Res.*, *117*. doi: 10.1029/2011JD016305

Fritts, D. C., Janches, D., & Hocking, W. K. (2010). Southern Argentina Agile Meteor Radar: Initial assessment of gravity wave momentum fluxes. *J. Geophys. Res.*, *115*. doi: 10.1029/2010JD013891

Fritts, D. C., Janches, D., Hocking, W. K., Mitchell, N. J., & Taylor, M. J. (2012b). Assessment of gravity wave momentum flux measurement capabilities by meteor radars having different transmitter power and antenna configurations. *J. Geophys. Res.*, *117*(D10108). doi: 10.1029/2011JD017174

He, M., Chau, J. L., Stober, G., Hall, C. M., Tsutsumi, M., & Hoffmann, P. (2017). Application of Manley-Rowe relation in analyzing nonlinear interactions between planetary waves and the solar semidiurnal tide during 2009 sudden stratospheric warming event. *J. Geophys. Res.: Space Phys.*, *122*(10), 10,783-10,795. doi: 10.1002/2017JA024630

Hines, C. O. (1988). A modeling of atmospheric gravity waves and wave drag generated by isotropic and anisotropic terrain. *J. Atmos. Sci.*, *45*, 309–322.

Hocking, W. K. (2005). A new approach to momentum flux determinations using SKiYMET meteor radars. *Annales Geophysicae*, *23*(7), 2433–2439. doi: 10.5194/angeo-23-2433-2005

Hocking, W. K., Fuller, B., & Vandepeer, B. (2001). Real-time determination of meteor-related parameters utilizing modern digital technology. *J. Atmos. Sol.-Terr. Phy.*(63), 155–169. doi: 10.1016/S1364-6826(00)00138-3

Hocking, W. K., & Thayaparan, T. (1997). Simultaneous and collocated observations of winds and tides by MF and meteor radars over london, canada (43°N, 81°W), during 19941996. *Radio Science*, *32*(2), 833–865.

Hoffmann, P., Becker, E., Singer, W., & Placke, M. (2010). Seasonal variation of mesospheric waves at northern middle and high latitudes. *J. Atmos. Sol.-Terr. Phy.*, *72*(14-15), 1068–1079. doi: 10.1016/j.jastp.2010.07.002

Holdsworth, D. A., Reid, I. M., & Cervera, M. A. (2004). Buckland park allsky interferometric meteor radar. *Radio Sci.*, *39*(5). doi: 10.1029/2003RS003014

Jacobi, C., Portnyagin, Y. I., Solovjova, T. V., Hoffmann, P., Singer, W., Fahrutdinova, A. N., ... Meek, C. E. (1999). Climatology of the semidiurnal tide at 5256°N from ground-based radar wind measurements 19851995. *J. Atmos. Sol.-Terr. Phy.*, *61*(13), 975–991. doi: 10.1016/S1364-6826(99)00065-6

Jia, M., Xue, X., Gu, S., Chen, T., Ning, B., Wu, J., ... Dou, X. (2018). Multiyear observations of gravity wave momentum fluxes in the midlatitude mesosphere and lower thermosphere region by meteor radar. *J. Geophys. Res.*, *123*, 5684–5703. doi: 10.1029/2018JA025285

Jones, J., Webster, A. R., & Hocking, W. K. (1998). An improved interferometer design for use with meteor radars. *Radio Sci.*, *33*, 55–65. doi: 10.1029/97RS03050

Kudeki, E., & Franke, S. J. (1998). Statistics of momentum flux estimation. *J. Atmos. Sol.-Terr. Phy.*, *60*, 1549–1553.

Kumar, K. K., Subrahmanyam, K. V., Mathew, S. S., Koushik, N., & Ramkummar, G. (2018). Simultaneous observations of the quasi 2-day wave climatology over the low and equatorial latitudes in the mesosphere lower thermosphere. *Clim. Dyn.*, *51*, 221–233. doi: 10.1007/s00382-017-3916-2

Laskar, F. I., Chau, J. L., Stober, G., Hoffmann, P., Hall, C. M., & Tsutsumi, M. (2016). Quasi-biennial oscillation modulation of the middle- and high-latitude mesospheric semidiurnal tides during AugustSeptember. *J. Geophys. Res.: Space Phys.*, *121*(5), 4869–4879. doi: 10.1002/2015JA022065

Lindzen, R. S., & Chapman, S. (1969). Atmospheric tides. *Space Sci. Rev.*, *10*, 3–188.

Liu, A. Z., Lu, X., & Franke, S. J. (2013). Diurnal variation of gravity wave momentum flux and its forcing on the diurnal tide. *J. Geophys. Res.*, *118*, 1668–1678.

Liu, H.-L., & Roble, R. G. (2002). A study of a self-generated stratospheric sudden warming and its mesospheric-lower thermospheric impacts using the coupled TIME-GCM/CCM3. *J. Geophys. Res.*, *107*. doi: 10.1029/2001JD001533

Lund, T., Fritts, D., Kam, W., Laughman, B., & Liu, H.-L. (2020). Numerical simulation of mountain waves over the Southern Andes, Part 1: Mountain wave and secondary wave character, evolutions, and breaking. *J. Atm. Sci.*.

McCormack, J. P., Coy, L., & Singer, W. (2014). Intraseasonal and interannual variability of the quasi 2 day wave in the Northern Hemisphere summer mesosphere. *J. Geophys. Res. Atmos.*, *119*, 2928–2946. doi: 10.1002/2013JD020199

Meriwether, J., Faivre, M., Fesen, C., Sherwood, P., & Veliz, O. (2008). New results on equatorial thermospheric winds and the midnight temperature maximum. *Ann. Geophys.*, *26*, 447–466.

Murphy, D. J., Forbes, J. M., Walterscheid, R. L., Hagan, M. E., Avery, S. K., Aso, T., … Vincent, R. A. (2006). A climatology of tides in the antarctic mesosphere and lower thermosphere. *J. Geophys. Res.*, *111*. doi: 10.1029/2005JD006803

Offermann, D., Hoffmann, P., Knieling, P., Koppmann, R., Oberheide, J., Riggin, D. M., … Steinbrecht, W. (2011). Quasi 2 day waves in the summer mesosphere: Triple structure of amplitudes and longterm development. *J. Geophys. Res.*, *116*. doi: 10.1029/2010JD015051

Orte, P. F., Wolfram, E., Salvador, J., Mizuno, A., Bègue, N., Bencherif, H., … Quiroga, J. (2019). Analysis of a southern sub-polar short-term ozone variation event using a millimetre-wave radiometer. *Ann. Geophys.*, *37*, 613–629. doi: 10.5194/angeo-37-613-2019

Pancheva, D., & Mukhtarov, P. (2011). Atmospheric tides and planetary waves: recent progress based on SABER/TIMED temperature measurements (20022007). *Aeronomy of the Earths Atmosphere and Ionosphere, IAGA Special Sopron Book Series 2*. doi: 10.1007/978-94-007-0326-1_2

Piani, C., Durran, D., Alexander, M. J., & Holton, J. R. (2000). A numerical study of three-dimensional gravity waves triggered by deep tropical convection and their role in the dynamics of the QBO. *J. Atmos. Sci.*, *57*, 3689–3702. doi: 10.1029/2019EA000570

Placke, M., Hoffmann, P., Becker, E., Jacobi, C., Singer, W., & Rapp, M. (2011b). Gravity wave momentum fluxes in the MLTPart II: Meteor radar investigations at high and midlatitudes in comparison with modeling studies. *J. Atmos. Sol. Terr. Phys.*, *73*, 911–920. doi: 10.1016/j.jastp.2010.05.007

Placke, M., P. Hoffmann, P., Latteck, R., & Rapp, M. (2015). Gravity wave momentum fluxes from MF and meteor radar measurements in the polar MLT region. *J. Geophys. Res.*, *120*, 736–750. doi: 10.1002/2014JA020460

Placke, M., Stober, G., & Jacobi, C. (2011a). Gravity wave momentum fluxes in the MLTPart I: seasonal variation at Collm (51.3°N, 13.0°E). *J. Atmos. Sol. Terr. Phys.*, *73*, 904–910. doi: 10.1016/j.jastp.2010.05.007

Rossby, C.-G. (1939). Relation between variations in the intensity of the zonal circulation of the atmosphere and the displacements of the semipermanent centers of action. *J. Mar. Res.*, *2*, 38–55.

Sandford, D. J., Muller, H. G., & Mitchell, N. J. (2006). Observations of lunar tides in the mesosphere and lower thermosphere at Arctic and middle latitudes. *Atmos. Chem. Phys.*, *6*, 4117–4127.

Siddiqui, T. A., Maute, A., Pedatella, N., Yamazaki, Y., Lühr, H., & Stolle, C. (2018). On the variability of the semidiurnal solar and lunar tides of the equatorial electrojet during sudden stratospheric warmings. *Ann. Geophys.*, *36*,

1545–1562. doi: 10.5194/angeo-2018-80
Smith, A. K. (2012). Global dynamics of the MLT. *Surveys in Geophysics*, *33*(6), 1177–1230.
Spargo, A. J., Reid, I. M., & MacKinnon, A. D. (2019). Multistatic meteor radar observations of gravity-wavetidal interaction over southern Australia. *Atmospheric Measurement Techniques*, *12*, 4791–4812. doi: 10.5194/amt-12-4791-2019
Stening, R. J., Forbes, J. M., Hagan, M. E., & Richmond, A. D. (1997). Experiments with a lunar atmospheric tidal model. *J. Geophys. Res.*, *102*, 13,465–13,472. doi: 10.1029/97JD00778
Stober, G., & Chau, J. L. (2015). A multistatic and multifrequency novel approach for specular meteor radars to improve wind measurements in the mlt region. *Radio Sci.*, *50*, 431–442. doi: 10.1002/2014RS005591
Thorsen, D., Franke, S. J., & Kudeki, E. (1997). A new approach to MF radar interferometry for estimating mean winds and momentum flux. *Radio Sci.*, *32*(2), 707–726.
Trinh, Q. T., Ern, M., Doornbos, E., Preusse, P., & Riese, M. (2018). Characteristics of the quiettime hot spot gravity waves observed by GOCE over the Southern Andes on 5 July 2010. *Ann. Geophys.*, *36*, 425–444. doi: 10.5194/angeo-36-425-2018
Urco, J. M., Chau, J. L., Milla, M. A., Vierinen, J., & Weber, T. (2018). Coherent MIMO to improve aperture synthesis radar imaging of field-aligned irregularities: First results at Jicamarca. *IEEE Transactions on Geoscience and Remote Sensing*, *PP*(99), 1–11. doi: 10.1109/TGRS.2017.2788425
Urco, J. M., Chau, J. L., Weber, T., & Latteck, R. (2019). Enhancing the spatiotemporal features of polar mesosphere summer echoes using coherent MIMO and radar imaging at MAARSY. *Atmospheric Measurement Techniques*, *12*, 955–969. doi: 10.5194/amt-12-955-2019
Vadas, S. L., & Becker, E. (2019). Numerical modeling of the generation of tertiary gravity waves in the mesosphere and thermosphere during strong mountain wave events over the Southern Andes. *J. Geophys. Res.*, *124*, 7687–7718. doi: 10.1029/2019JA026694
Vadas, S. L., Xu, S., Yue, J., Bossert, K., Becker, E., & Baumgarten, G. (2019a). Characteristics of the quiettime hot spot gravity waves observed by GOCE over the Southern Andes on 5 July 2010. *J. Geophys. Res.*, *124*, 7034–7061. doi: 10.1029/2019JA026693
Vierinen, J., Chau, J. L., Charuvil, H., Urco, J. M., Clahsen, M., Avsarkisov, V., ... Volz, R. (2019). Observing mesospheric turbulence with specular meteor radars: A novel method for estimating second-order statistics of wind velocity. *Earth and Space Science*, *6*, 1171–1195. doi: 10.1029/2019EA000570
Vierinen, J., Chau, J. L., Pfeffer, N., Clahsen, M., & Stober, G. (2016). Coded continuous wave meteor radar. *Atmospheric Measurement Techniques*, *9*(2), 829–839.
Vincent, R. A., Kovalam, S., Reid, I. M., & Younger, J. P. (2010). Gravity wave flux retrievals using meteor radars. *Geophys. Res. Lett.*, *37*. doi: 10.1029/2010GL044086
Wilhelm, S., Stober, G., & Brown, P. (2019). Climatologies and long-term changes in mesospheric wind and wave measurements based on radar observations at high and mid latitudes. *Ann. Geophys.*, *37*, 851–875. doi: 10.5194/angeo-37-851-2019
Yamazaki, Y., Matthias, V., Miyoshi, Y., Stolle, C., Siddiqui, T., Kervalishvili, G., ... Alken, P. (2020). September 2019 antarctic sudden stratospheric warming: Quasi-6-day wave burst and ionospheric effects. *Geophys. Res. Lett.*, *47*. doi: 10.1029/2019GL086577

**Figure 1.**

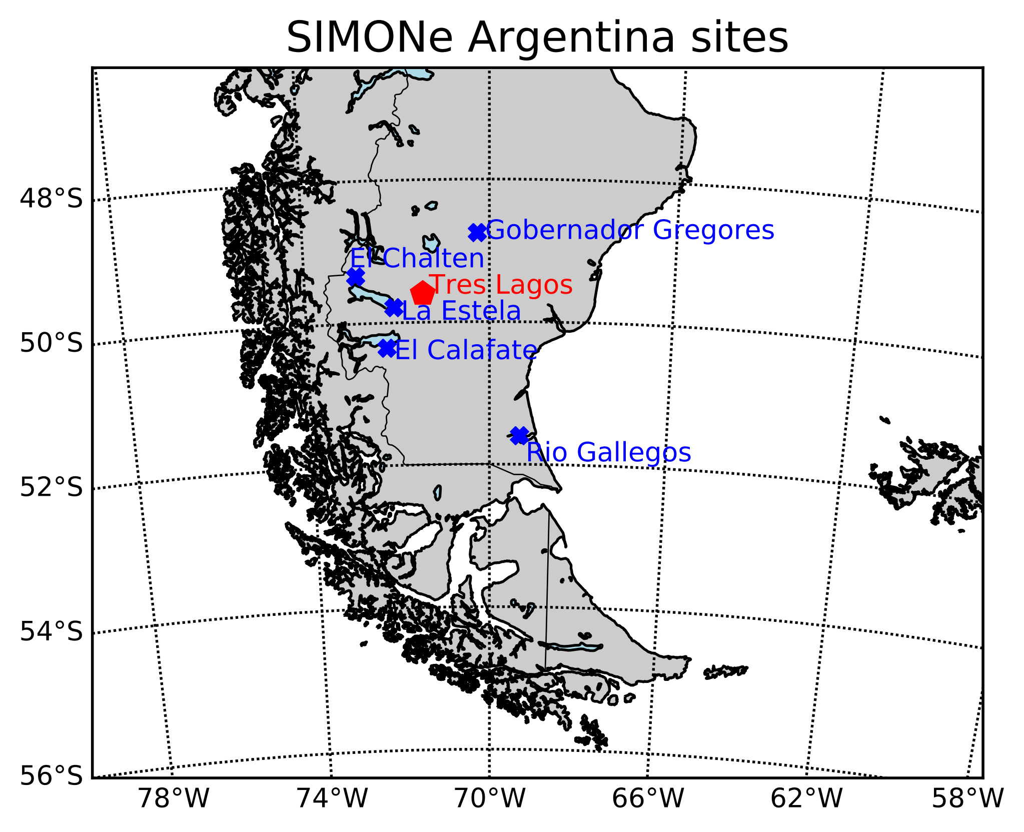

SIMONe Argentina sites
Gobernador Gregores
El Chalten
Tres Lagos
La Estela
El Calafate
Rio Gallegos
48°S
50°S
52°S
54°S
56°S
78°W
74°W
70°W
66°W
62°W
58°W

**Figure 2.**

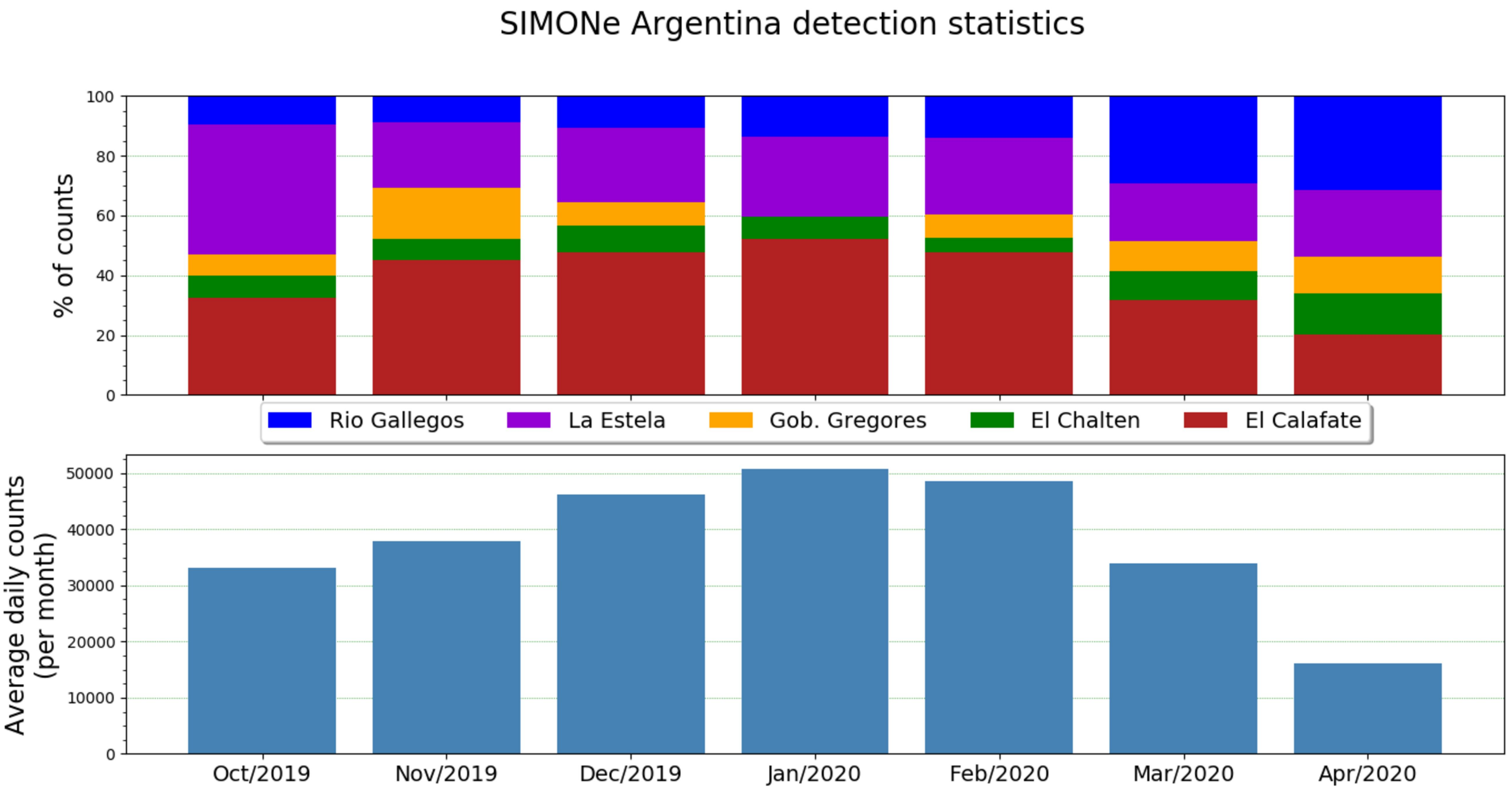
SIMONe Argentina detection statistics
% of counts
100
80
60
40
20
0
Rio Gallegos
La Estela
Gob. Gregores
El Chalten
El Calafate
Average daily counts
(per month)
50000
40000
30000
20000
10000
0
Oct/2019
Nov/2019
Dec/2019
Jan/2020
Feb/2020
Mar/2020
Apr/2020

**Figure 3.**

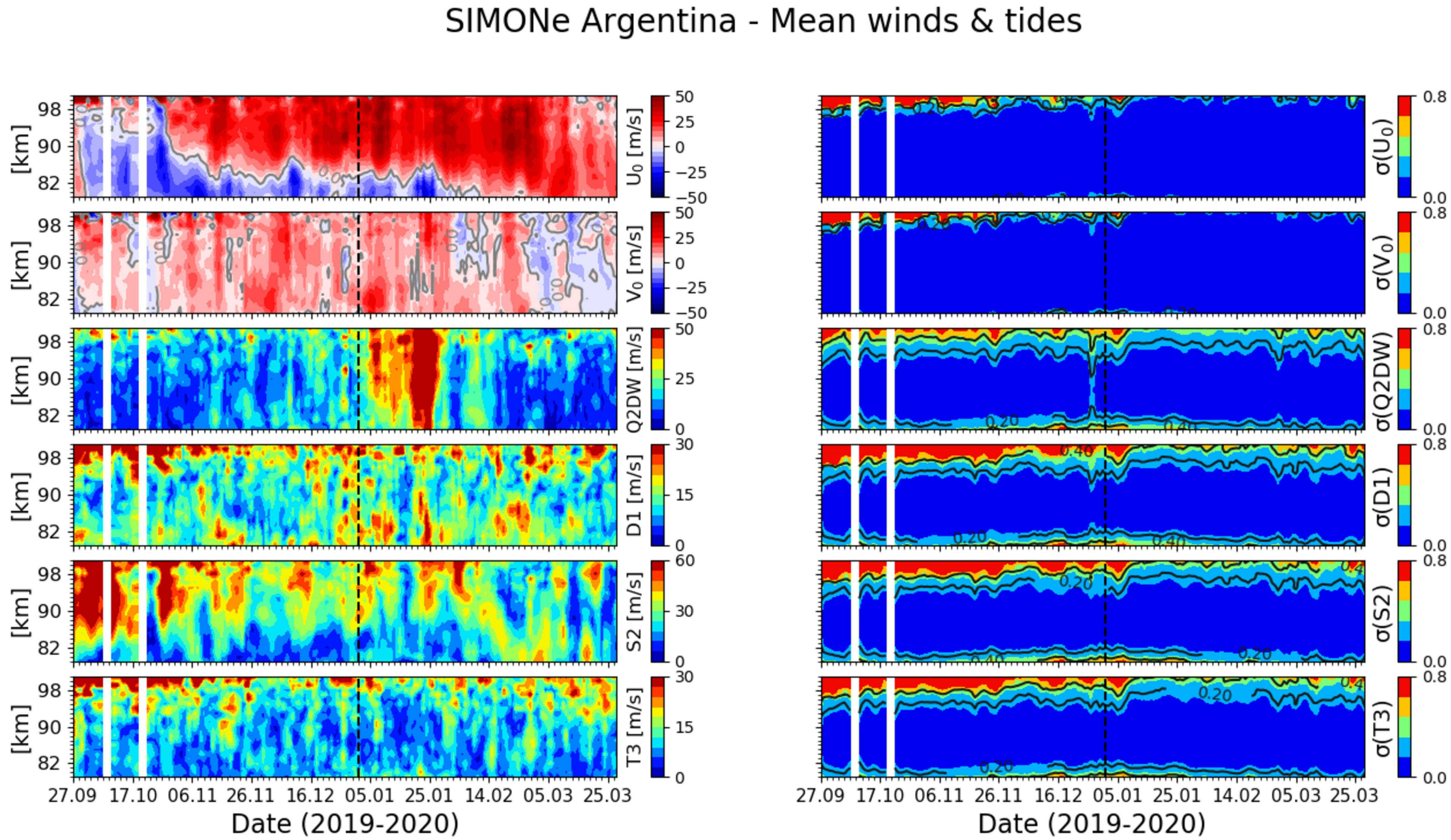

SIMONe Argentina - Mean winds & tides
[km]
98
90
82
$U_0$ [m/s]
$V_0$ [m/s]
Q2DW [m/s]
D1 [m/s]
S2 [m/s]
T3 [m/s]
50
25
0
−25
−50
30
15
60
σ($U_0$)
σ($V_0$)
σ(Q2DW)
σ(D1)
σ(S2)
σ(T3)
0.8
0.0
0.20
0.40
27.09
17.10
06.11
26.11
16.12
05.01
25.01
14.02
05.03
25.03
Date (2019-2020)

**Figure 4.**

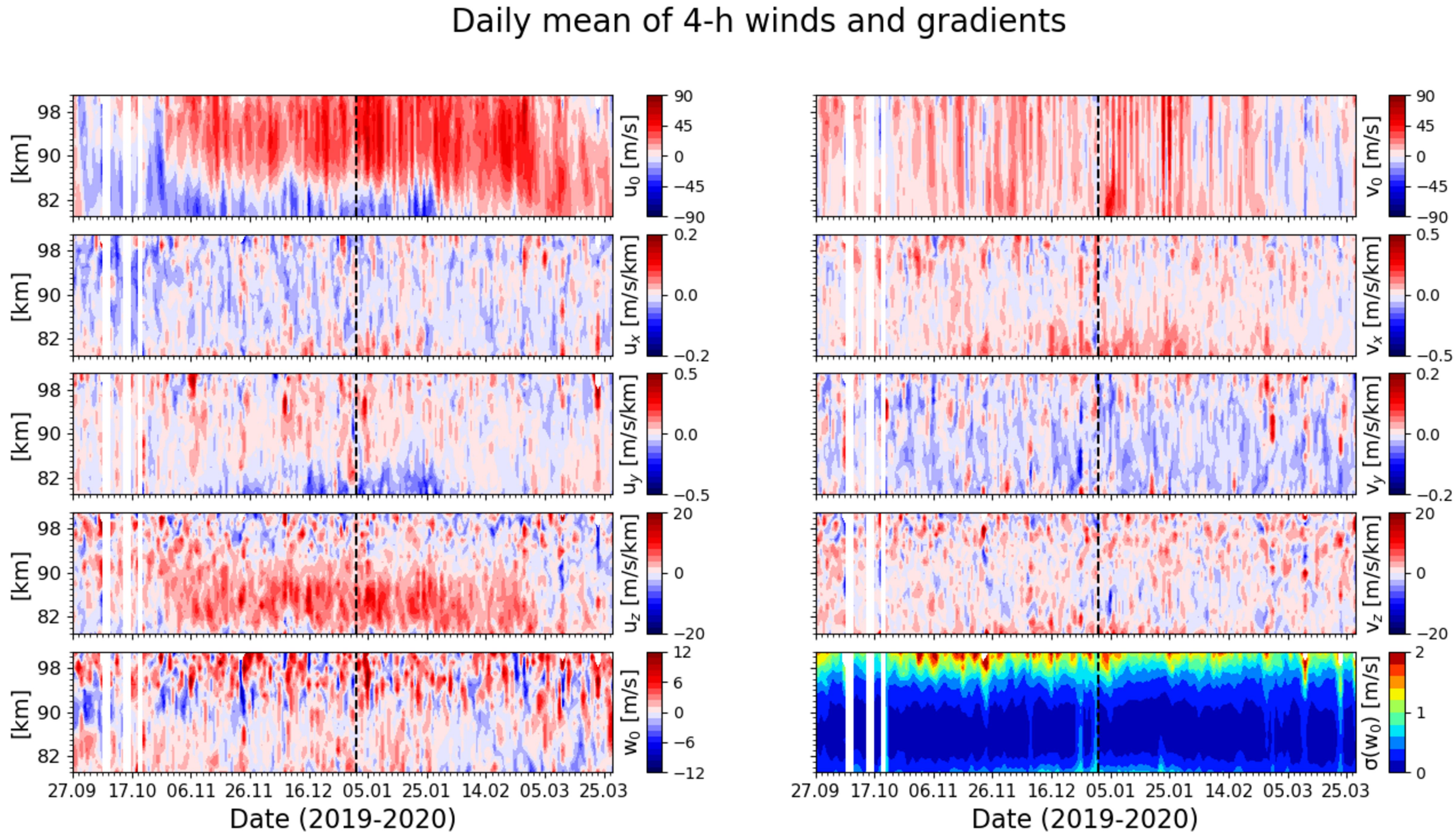

Daily mean of 4-h winds and gradients
[km]
98
90
82
u0 [m/s]
90
45
0
−45
−90
v0 [m/s]
ux [m/s/km]
0.2
0.0
−0.2
vx [m/s/km]
0.5
0.0
−0.5
uy [m/s/km]
vy [m/s/km]
uz [m/s/km]
20
0
−20
vz [m/s/km]
w0 [m/s]
12
6
0
−6
−12
σ(w0) [m/s]
2
1
0
27.09
17.10
06.11
26.11
16.12
05.01
25.01
14.02
05.03
25.03
Date (2019-2020)

**Figure 5.**

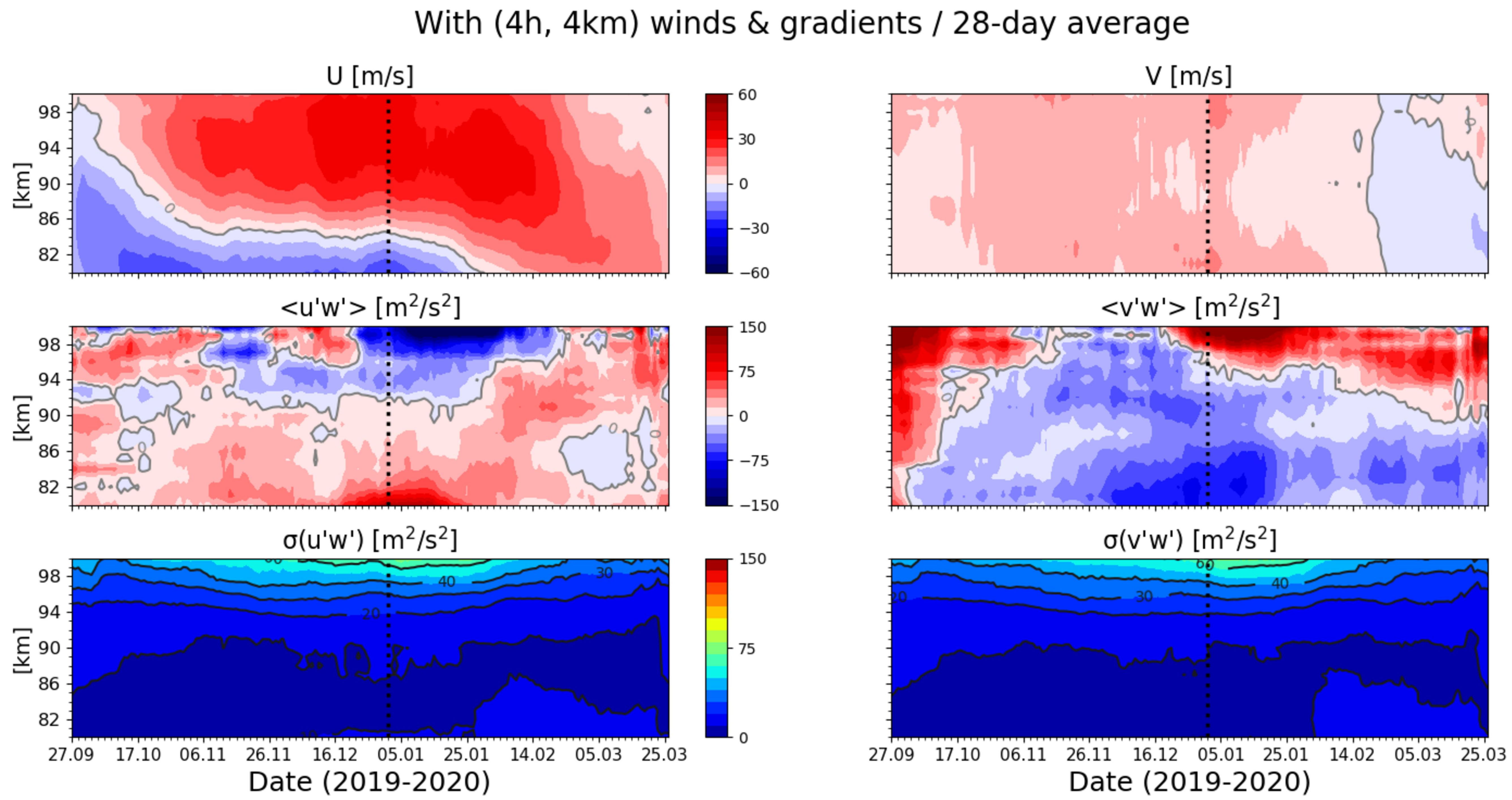

With (4h, 4km) winds & gradients / 28-day average
U [m/s]
V [m/s]
<u'w'> [m²/s²]
<v'w'> [m²/s²]
σ(u'w') [m²/s²]
σ(v'w') [m²/s²]
[km]
98
94
90
86
82
60
30
0
−30
−60
150
75
−75
−150
20
30
40
60
27.09
17.10
06.11
26.11
16.12
05.01
25.01
14.02
05.03
25.03
Date (2019-2020)